

CFD-Based Optimization of Hot Primary-Air Pipe Networks in Power Plant Milling Systems

Qingyun Yan¹, You Li², Yuanhong Zhu³, Kui Cheng³, Xueli Huang³, Cong Qi³ and Xuemin Ye^{2,*}

¹Jiangxi Vocational and Technical College of Electricity, Nanchang, 330032, China

²North China Electric Power University, Baoding, 071003, China

³Power China Jiangxi Electric Power Engineering Co., Ltd., Nanchang, 330096, China

*Corresponding Author: Xuemin Ye. Email: yexuemin@163.com

Received: 14 January 2020; Accepted: 08 April 2020

Abstract: A hot primary-air pipe system is the bridge connecting an air-preheater with a coal mill in power generation stations. The effective geometrical configuration of the pipe network greatly affects the air flow distribution and consequently influences the safe and economic operation of milling systems in power stations. In order to improve the properties of the air flow, in the present work the SIMPLEC method is used to simulate numerically the flow field for the original layout of the system. As a result, the internal mechanisms influencing the uneven pressure drop in each branch are explored and three optimization schemes are proposed accordingly. The numerical results indicate that, for the original layout, the local pressure drop of the tee section accounts for approximately 74% of the total drop of the system, with other pressure drops depending on the specific branch considered. It is shown that after optimization, a roughly balanced flow resistance and flow rate can be obtained. Compared with the original layout, the pressure drop relating to different branches is significantly reduced.

Keywords: Hot primary-air pipe; flow dynamics; layout optimization; numerical simulation

1 Introduction

A hot primary-air pipe system is the bridge connecting an air-preheater with a coal mill in power generation stations. The flow resistance of the system has an extremely important effect on the flow distribution in each branch pipe and then influences the safe and economic operation of combustion systems. As all branches in hot primary-air pipe systems are distinctly different in the space direction and pipe length, when throttle valves are fully opened, an obviously uneven flow distribution in each branch is observed in practical applications. To address this issues, the flow allocation in all branches is commonly achieved with the regulation of throttle valves, which definitely increases the local minor losses and energy consumption of the system, leading to an economic penalty to a certain extent. Generally, a hot primary-air pipe system contains different types of tees, e.g., shunt tees and confluence tees, and more importantly, the flow regimes in the upstream tees have a significant impact on the flow distribution of downstream branches. Consequently, it is of great significance to investigate the flow



This work is licensed under a Creative Commons Attribution 4.0 International License, which permits unrestricted use, distribution, and reproduction in any medium, provided the original work is properly cited.

dynamics and flow resistance of the hot primary-air pipe systems and then to optimize the layout, thereby reducing the feature of uneven flow resistance and improving the efficiency of fluid transportation. Recently, computational fluid dynamics has been widely used in pipeline design and optimization due to the notable advantages of fast calculation speed, strong flexibility, and reliable results [1–3].

Presently, many reports have been carried out on the flow characteristics of parallel pipe systems. Zhang et al. [4] applied a numerical method to investigate the influence of inlet Reynolds number, tube spacing, area ratio, and outlet branch quantity on the uniformity of parallel pipeline flow. They found that under the same inlet flow rate, the increase in the outlet quantity leads to an obvious unevenness of flow distribution. Kou et al. [5] pointed out that the local resistance of the T-like pipe network decreases with increasing branch pipe length ratio and branch quantity. Zhou et al. [6] simulated the flow distribution of each circular branch pipe in a heat exchanger and found that for different arrangements of parallel pipelines, changing the diameter and spacing of tubes can improve the uniformity of flow distribution. In the investigation of a parallel cooling channel of an engine, Jiang et al. [7] discussed the influence of heat transfer characteristics and the cross-section shape on flow distribution and obtained the best flow distribution with the utilization of a triangular cross-section. Using the similar criteria, Li et al. [8] carried out tunnel ventilation experiments and found that the resistance coefficient of the tunnel is greatly affected by the air volume and the pipeline layout, while the local resistance coefficients at inlets and exits are only greatly affected by the pipeline layout. Zhang et al. [9] arranged a guide vane in the parallel pipe to reduce the local resistance of branch pipes and determined the best pattern and position of the guide vane.

The shape of a tee has a crucial impact on the flow distribution of hot primary-air pipes. Costa et al. [10] performed an experiment on the round and sharp 90° tees and found that the local resistance of a branch pipe is higher than that of the main pipe, and the recirculation area in the branch pipe with round tee is small, thereby diminishing the local resistance. Benes et al. [11] employed the EARS model to simulate the influence of square and circular tees and obtained the internal pressure distribution. They found that the mean pressure distribution along channels exhibits correct qualitative behavior and can be used for the loss coefficient estimation. Based on experimental and numerical investigation, Li et al. [12] pointed out that installing a wedge-shaped component of appropriate height in the tee and elbow can reduce the local losses. Gao et al. [13] installed a guide vane at the tee to reduce the minor losses and discussed the installation position and type of the guide vane. They found that the tee installed with a new guide vane reduces the fluid deformation and the turbulence energy dissipation, and diminishes the amount of mechanical energy convert to the internal energy.

Presently, few studies on the flow resistance and distribution of combined tees in parallel pipe systems have been reported so far. Therefore, for an actual hot primary-air pipe system inclusive of the combined tees, the present study is aimed to investigate the influence of the upstream pipe layout on the downstream flow dynamics and resistance, and then propose three optimization schemes, finally provide the best scheme for the design and optimization of the complex parallel pipe systems.

2 Numerical Methodology

2.1 Physical Model

Fig. 1 depicts a three-dimensional model of a hot primary-air pipe system. The air heated by an air preheater enters the inlets 1 and 2, then passes a header through the square-section elbow, square joint and round-section elbow. Next, the air is distributed to each branch A, B, C, D, and E, and finally is transported to a coal pulverizer. The operating conditions and parameters under different loads are presented in Tab. 1. The working condition of BMCR (Boiler maximum continuous rating) with the checked coal is selected to examine and optimize the original layout. Both two inlets have the same velocity and the air temperature of 370°C. For the convenience of subsequent discussion, the fluid from the inlet 1 to the outlet A is called branch A, and similarly, branch B, branch C, branch D, and branch E. The main geometrical parameters are listed in Tab. 2.

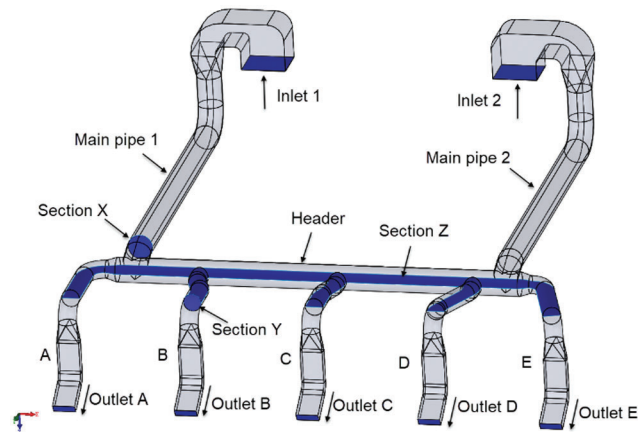


Figure 1: Geometric model of hot primary air duct

Table 1: Main parameters in the hot primary air pipe system

Coal type	Load	Operating condition	Inlet velocity (m/s)
Check coal	BMCR	2 inlets, 5 outlets	8.04
	BRL	2 inlets, 5 outlets	7.84
Design coal	BMCR	2 inlets, 4 outlets	6.40
	BRL	2 inlets, 4 outlets	6.23
	75% BMCR	2 inlets, 3 outlets	4.74
	50% BMCR	1 inlet, 2 outlets	6.49
	30% BMCR	1 inlet, 2 outlets	5.10

Note: BRL-boiler rated load

Table 2: Geometrical parameters of the hot primary air pipe system

Type	Name	Parameters type	Dimensions (mm)
Section	Inlet	Length × width	3,252 × 2,812
	Main pipe/header	Diameter	1,812
	Branch pipe	Diameter	1,312
	Outlet B	Length × width	1,630 × 600
Pipe length	Inlet 1 to section X	Length	36,626
	section X to section Y	Length	12,761
	section Y to outlet B	Length	9,166

2.2 Numerical Method and Boundary Conditions

The 3D model of the pipe system was meshed using ICEM, as shown in Fig. 2. To improve the calculation accuracy and speed, the structured grid is generated by the block division, and the grid quality is refined by using the O-type division. The final grid quality is beyond 0.5. A standard wall function is adopted in the near-wall region [9], so the influence of the first layer grid height on the simulation needs to be considered. Taking $y^+ = 30$, the first layer grid height is 1.4 mm. Considering the complexity of the

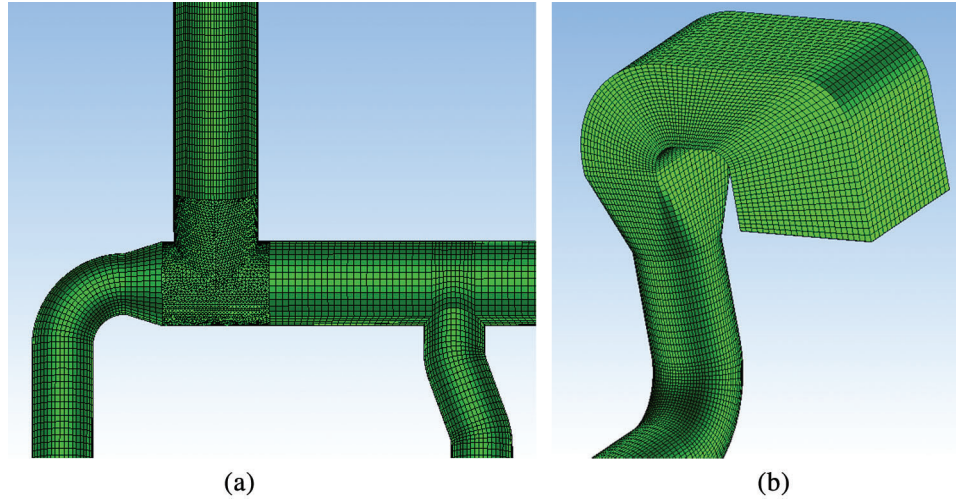


Figure 2: Grid of a hot primary-air pipe. (a) T-junction and (b) Elbow

physical model, the unstructured meshing was performed at the tees. The transmission and exchange of data were achieved with the Interface.

Fluent 17.0 is applied to solve the steady-3D continuity and Reynolds averaged Navier-Stokes (RANS) equations. Considering that the flow passing the tee and elbow is complicated and the strong swirl flow and secondary flow are evolved, the Realizable k - ϵ turbulence model is selected [9,14,15]. Based on the assumption of the quasi-steady turbulence, the present numerical calculation is conducted with a steady-state solver. To satisfy the higher calculation accuracy requirements, the pressure terms are addressed with the second-order discretization, and the momentum equation, turbulent kinetic energy, and turbulent dissipation rate equation are discretized with the second-order upwind scheme [15]. The SIMPLEC algorithm is used to address the pressure-velocity coupling [16]. When the residual of each parameter is less than 10^{-4} , and the deviation between the inlet and outlet flow rate is less than 0.1%, the present simulation is considered to be convergent [14,15,17].

The governing equations including the steady-3D continuity, RANS equations and Realizable k - ϵ turbulence model, are stated as follows:

$$\frac{\partial \bar{u}_i}{\partial x_i} = 0 \quad (1)$$

$$\rho \bar{u}_j \frac{\partial \bar{u}_i}{\partial x_j} = -\frac{\partial \bar{p}}{\partial x_i} + \mu \frac{\partial^2 \bar{u}_i}{\partial x_j \partial x_j} + \frac{\partial}{\partial x_j} (-\rho \overline{u'_i u'_j}) \quad (2)$$

$$\rho \frac{\partial (k \bar{u}_i)}{\partial x_i} = \frac{\partial}{\partial x_j} \left[\left(\mu + \frac{\mu_t}{\sigma_k} \right) \frac{\partial k}{\partial x_j} \right] + G_k - \rho \epsilon \quad (3)$$

$$\rho \frac{\partial (\epsilon \bar{u}_i)}{\partial x_i} = \frac{\partial}{\partial x_j} \left[\left(\mu + \frac{\mu_t}{\sigma_\epsilon} \right) \frac{\partial \epsilon}{\partial x_j} \right] + \rho C_1 E \epsilon - \rho C_2 \frac{\epsilon^2}{k + \sqrt{v \epsilon}} \quad (4)$$

where, \bar{u}_i and u'_i are the time-averaged and fluctuating velocity components in the i -direction, respectively; \bar{p} is the time-averaged static pressure, x_i is the spatial coordinate, ρ and μ are the liquid density and dynamic viscosity, respectively; k and ϵ are turbulent kinetic energy and dissipation rate, respectively; σ_k and σ_ϵ are the turbulent Prandtl numbers for k and ϵ , respectively, $\sigma_k = 1.0$, $\sigma_\epsilon = 1.2$; G_k is the production of turbulent kinetic

energy due to mean velocity gradient, $G_k = -\rho \overline{u'_i u'_j} \frac{\partial \bar{u}_i}{\partial x_j}$. $C_1 = \max\left(0.43, \frac{\psi}{\psi + 5}\right)$, where $\psi = Ek/\epsilon$, E is the mean rate-of-strain tensor, $E = \sqrt{2E_{ij}E_{ij}}$; $C_2 = 1.9$.

The boundary condition of the inlet is set to the velocity inlet, and the airflow direction is perpendicular to the inlet cross-section. The turbulence definition method selects the turbulent intensity and hydraulic diameter [9], where the hydraulic diameter is the characteristic length of the pipe inlet, and the turbulent intensity (I) is solved using $I = 0.16 \times \text{Re}^{-1/8}$, where Re is the Reynolds number. The outlet boundary condition is set to the pressure-outlet, and the target flow rate is set to the value under the BMCR operating condition. The turbulence is defined in the same way as the inlet. The operating pressure is the standard atmospheric pressure, and the reference point is located at the center point of the outlet of branch B. A non-slip condition is employed at all wall conditions, that is, the fluid velocity close to the wall is zero [18]. The material of all pipes is set to new seamless steel pipe with the absolute roughness of 0.06 mm. The influence of the gravity on the simulated results is neglected.

To verify the reliability of the governing equations, the local pressure drop of a pipe tee with the diameter of 200 mm is performed, and the simulated results are in good agreement with the experimental results of Rahmeyer et al. [19] with the maximum relative error of 3.1%. Hence, the present model is feasible to predict the flow resistance in this study. Additionally, to verify the grid independence of the present simulation, the grid numbers of 0.86, 1.72, 2.89 and 3.78 million are performed for the original layout, as shown in Tab. 3. It can be seen that when the grid number is 2.89 million, the pressure drop in each branch pipe is very close to that of 3.78 million grids. Considering the calculation accuracy and duration, the model with a mesh number of 2.89 million is selected for the original layout. Other schemes also adopted this method to determine the final grid number.

Table 3: Total pressure drop of each branch under different grid numbers

Number of grids (million)	Total pressure drop in each branch pipe (Pa)				
	A	B	C	D	E
0.86	280.5	540.2	512.4	546.8	254.1
1.72	290.3	552.1	528.7	562.5	275.2
2.89	294.6	560.0	504.1	573.6	287.8
3.78	294.5	560.4	504.9	574.8	287.9

3 Results and Discussion

3.1 Original Layout

For the hot primary-air piping system studied in this study, due to the different lengths and spatial directions of branches, the pressure drop of each branch is different when throttle valves are fully opened, as indicated in Tab. 3. Therefore, throttle valves are regulated to achieve the flow balance of each branch in actual operation, leading to increased minor losses at the throttle valves [4]. The single-phase flow losses in a pipe system are composed of the friction losses and minor losses. The hot primary-air pipe system has a large diameter and a relatively short pipe length, hence the friction losses are small. Tab. 4 lists the total pressure drop of three sections. It can be observed that the losses at the tee, from section X to section Y, are the largest in the total losses, accounting for approximately 74% of the total losses, whereas the minor losses at the elbow accounts for 5%. Therefore, the modification of the tee is the most effective way to optimize the hot primary-air pipe system.

Table 4: Total pressure drop of three sections of the original layout

Pipe section	Total pressure drop (Pa)
inlet 1 to section X	71.9
section X to section Y	414.9
section Y to outlet B	73.3

The hot primary-air pipe system includes shunt and confluence tees, and the layout of upstream tees has an apparent impact on the flow regime in the downstream tees [4], as shown in Figs. 3 and 4. Fig. 3 indicates that the fluid from the main pipe 1 enters branches A, B, and C, and the fluid from the main pipe 2 enters branches C, D, and E. After the fluid passes from the main pipe to the header through a shunt tee, vortices are formed at the junction. And the flow direction is changed by impacting the header, and a pair of vortex is emerged in the vicinity of the inlet of branch D. The upper vortex is produced by the shunt tee, whereas the downside vortex is formed by the unbalanced distribution of the local flow at branch D. Branch D inlet is close to the main pipe 2, and part of the fluid flows directly from the main pipe 2 into branch D, while a small part of fluid is distributed into branch C. Compared with branch B, only an upper vortex is evolved in the vicinity of the inlet of branch B, which possibly results from the large distance from the shunt tee to Branch B. Branches B and D are connected to the header. When the fluid enters the branches, vortices are evolved on the downwind side. Due to the different layout of branches B and D, the shape and size of these vortices are different appreciably. The comparison illustrates that the size of the vortex at branch D is relatively large and its flow cross-area is relatively small, hence at the same flow rate, the velocity at branch D inlet is high, causing apparent local minor losses.

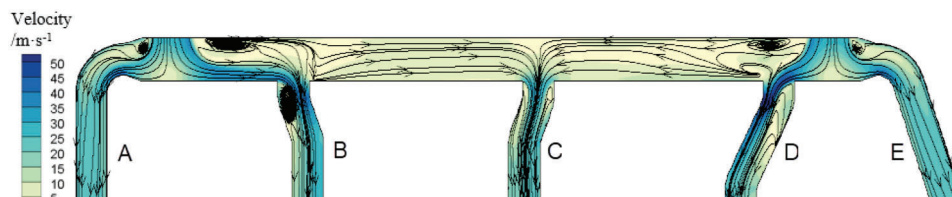
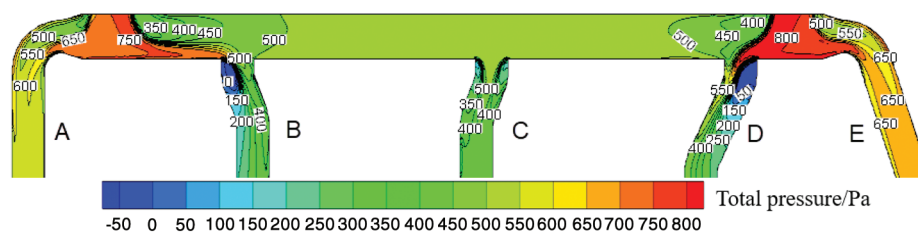
**Figure 3:** Streamline distribution of the Z-section of the original layout**Figure 4:** Total pressure distribution of the Z-section of the original layout

Fig. 4 shows that the total pressure distribution in the section of between branches B and D is uniform, the local friction losses from the branch B inlet to branch C inlet are 3 Pa and can be ignored. At the tee, however, the pressure gradient is notable, and a low-pressure zone is formed on the downwind side of the inlets of branches B and D. Compared with the downside of the tee, the pressure distribution in the inlet of branches B and D is distinctly non-uniform, and the pressure gradient at the tee inlet is high, e.g., for

branch B, the total pressure varying from 500 Pa to 0, and for branch D, the total pressure varying from 550 Pa to 50 Pa.

3.2 Optimization

In order to reduce the flow resistance of the system, the piping design is optimized on the premise that all throttle valves are fully opened, and is strived to achieve equal pressure drop in each branch. Then, throttle valves are used to equalize the flow distribution of each branch. According to the actual requirements of the equal flow distribution in each branch, this study is aimed to evaluate the pressure drop of each branch and optimize the original layout of the pipe system.

Tab. 3 shows that the flow resistance of branches A and E is small, whereas that of branches B, C and D is large. Based on the flow characteristics of the original layout, the arrangement of branches B, C, and D are optimized, as indicated in Fig. 5. Case 1 varies an angle of branches B and D from 90° to 65° and adjusts the elbow position of branch B, and the layout of branch C remains unchanged, as shown in Fig. 5b. For Case 2, the inlet of branch B with the angle of 70° is configured to close to the tee which avoiding the beam support, the connection of branch C is altered with a gradual expansion section, and the modification of branch D with an angle of 65° is the same as Case 1, as shown in Fig. 5c. Case 3 arranges an angle of 48° and 65° for branch B and branch D, respectively, and branch C is perpendicular to the header with a connection of a gradual expansion section, as shown in Fig. 5d.

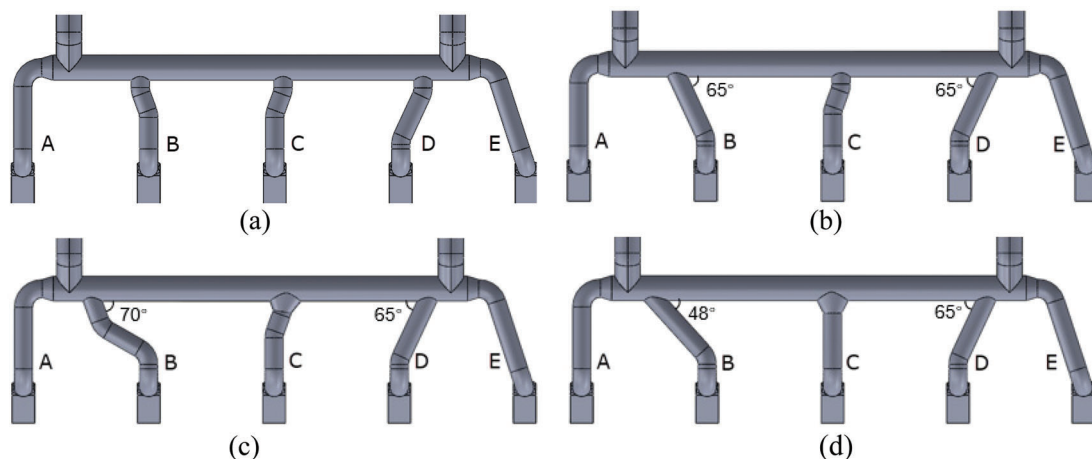


Figure 5: Diagram of the hot primary-air pipe system before and after optimization. (a) Original (b) Case 1 (c) Case 2 and (d) Case 3

Fig. 6 depicts the internal flow patterns of optimized layouts. It can be found that after optimizing the pipe system, the internal flow features are greatly improved, the size of the vortices at the branch inlet is significantly reduced, and the effective flow area increases. Among them, the flow regime in the header of Case 1 changes apparently and a circulation area is evolved between branches B and C. For Case 2, the flow regime in the header is roughly similar to the original one. The velocity is faster on the lower side between branches B and D. Influencing by the elbow, the center of a vortex in branch B moves towards downstream and the recirculation zone increases slightly, and the vortices at the inlet of branch C disappear roughly. For Case 3, the vortex in branch B also disappears roughly, and there is only a small range of low-speed zone at the inlet. Part of the fluid entering the header directly flows into branch B, thereby reducing the local minor losses. The flow field in branch C is uniform, and almost no vortices generate.

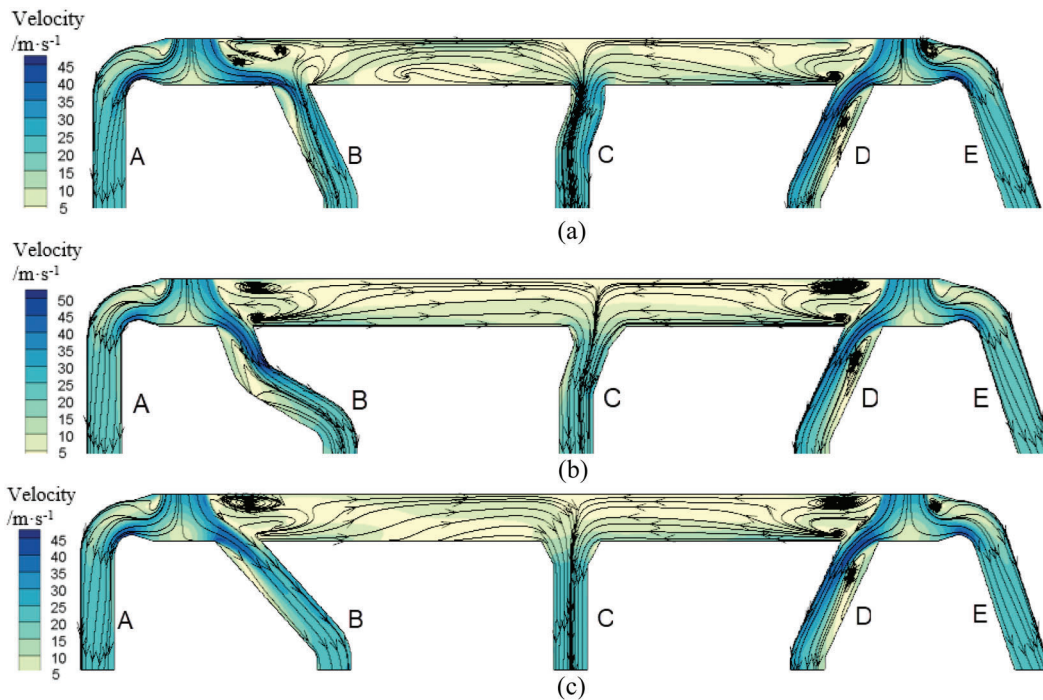


Figure 6: Streamline of Z-section after optimization. (a) Case 1 (b) Case 2 and (c) Case 3

Fig. 7 illustrates the total pressure distribution of the Z-section after optimization. For Case 1, the low-pressure zone at the inlets of both branches B and D are reduced, and the pressure gradient is diminished. The feature of uneven pressure distribution in the header remains, and different low-pressure zones are formed on both sides of branch C. For Case 2, the total pressure is symmetrically distributed at the left and right sides of the header. The low-pressure zone at branch B inlet is expanded and the pressure gradient is raised. For Case 3, a strip zone of high-pressure is observed at the middle of the header between branches C and D; a small low-pressure area is generated at branch C inlet and the uniform distribution of the total pressure is illustrated in the downstream. Additionally, the low-pressure zone at branch B inlet is shrunk significantly, but the pressure gradient perpendicular to the flow direction of branch B is increased.

3.3 Vorticity and Turbulent Energy Dissipation Distribution

Fig. 8 depicts the vorticity distribution of the Z-section at the inlet of branch B before and after optimization. For the original layout, the vorticity is high after the fluid flows into the header, and the fluid entering branch B generates a strong vortex on the left side. For Case 1, the vorticity on the left side of branch B is reduced. Due to the influence of the tee, the vorticity on the right side of branch B is slightly raised. For Case 2, part of the vortices enters the right side of branch B from the header. Because the angle between branch B and the header is large, the vorticity is notable on the left side of the inlet, leading to the flow resistance of branch B to be greater than Case 1. For Case 3, the vortex zone on the left side of the inlet is lessened, while the vortex zone on the right side increases, the reduced vorticity, however, causes the flow resistance of the pipe to decrease significantly.

The flow resistance can be described with the energy dissipation, which includes the viscous dissipation and turbulent dissipation due to velocity pulsations [20]. Fig. 9 shows the energy dissipation distribution of the Z-section at the inlet of branch B before and after optimization. The energy dissipation of the original layout is high compared with the optimized schemes, and the region of more than 4000 W/m^3 is found at the right of the inlet of branch B, which is mainly caused by the impact losses of the fluid. The energy

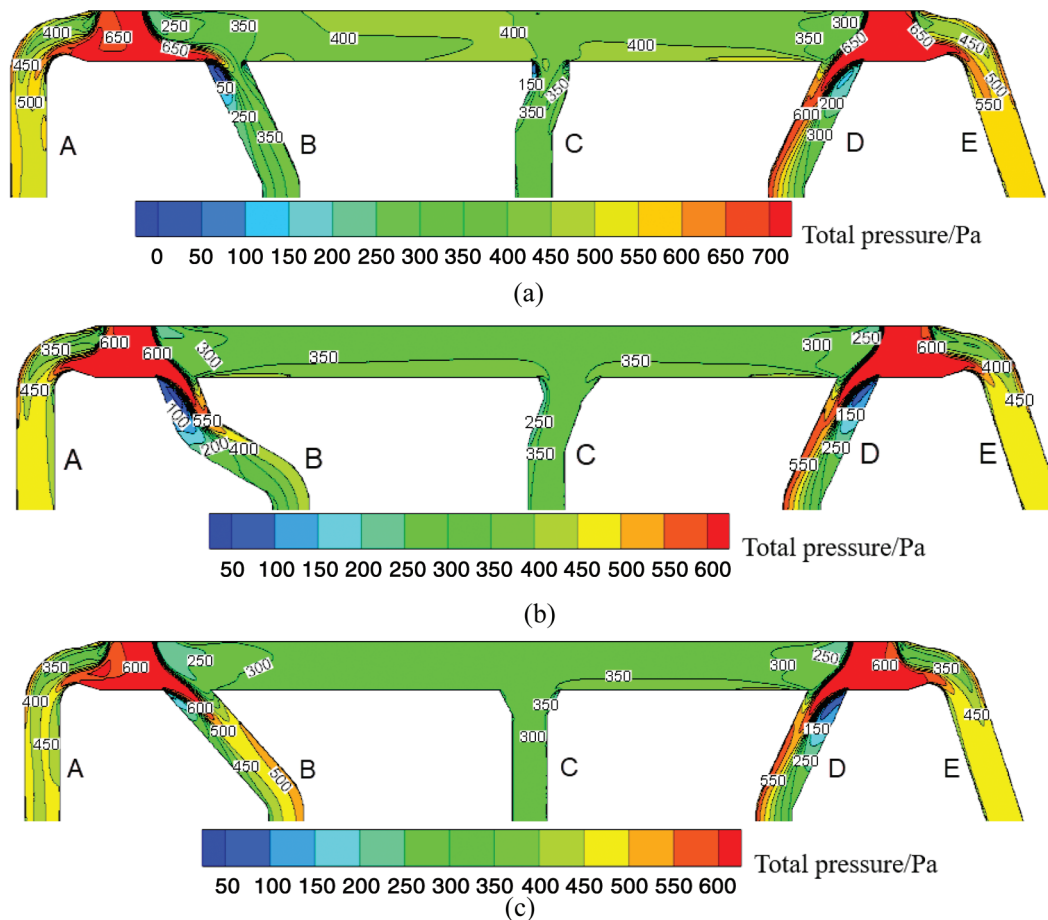


Figure 7: The total pressure distribution of Z-section after optimization. (a) Case 1 (b) Case 2 and (c) Case 3

dissipation at the main pipe inlet and at the left side of branch B is also remarkable, which mainly results from the vortex formed by the fluid flowing through the tee, as shown in Fig. 9a. After optimization, the energy dissipation is reduced to some extent. The energy dissipation gradient in Case 1 is diminished, as shown in Fig. 9b. For Cases 2 and 3, the energy dissipation on the right side of branch B inlet is reduced significantly, as shown in Figs. 9c and 9d. This is mainly because the branch inlet is close to the main pipe outlet, which allows the fluid to enter branch B directly, thereby reducing the impact losses. For Case 3, the energy dissipation at the left of branch B inlet is also reduced greatly, as shown in Fig. 9d.

As the configuration of branch C in Case 1 is the same as the original, the vorticity distribution in branch C is no longer discussed. Fig. 10 presents the vorticity distribution of the Z-section of branch C. The vortex zone and vorticity at the branch C inlet of the original layout are relatively large. After optimization with Cases 2 and 3, the vorticity decreases apparently. Case 3 has the best improvement and characterizes by significantly reduced vorticity. Considering the space limitation and flow direction change in the practical applications, an elbow is still used to vary the flow direction, so a small zone of the vortex is evitable at the elbow.

Fig. 11 depicts the energy dissipation distribution of the Z section at the inlet of branch C. It can be found that the energy dissipation in the original layout is mainly focused on branch C inlet, and the energy dissipation on the left is greater than that on the right, which is caused by the vortex evolved at the branch inlet [4,13] as shown in Fig. 11a. After optimization, the energy dissipation is decreased distinctly.

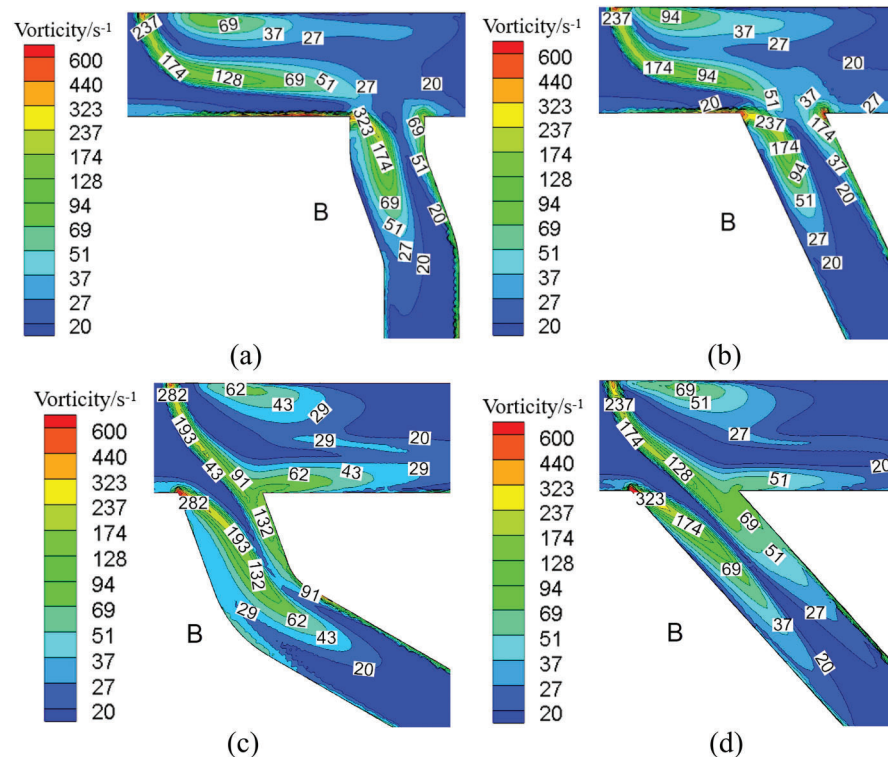


Figure 8: Vorticity distribution of Z-section at the inlet of branch B. (a) Original (b) Case 1 (c) Case 2 and (d) Case 3

The energy dissipation region of Case 3 is lessened significantly, and the reduced maximal energy dissipation leads to the reduction of energy losses, as shown in Fig. 11c.

As the configuration of branch D in Cases 2 and 3 is the same as that in Case 1, the following discussion examines the vortex distribution of branch D for the original and Case 1. Fig. 12 presents the vorticity distribution at the inlet of the Z-section before and after optimization. For the original layout, the inlet of branch D is almost full of vortices, part of which originates from the header and part of it is triggered by the flow turning into branch D, thus the flow resistance of branch D is greater than branch B. After optimization, the vorticity on the left side of the inlet is almost unchanged, while the vorticity on the right side is diminished significantly, thereby reducing the local resistance of branch D.

Fig. 13 displays the energy dissipation distribution of the Z-section at the inlet of branch D. The region of large energy dissipation in the original layout is concentrated in the middle and left side of branch D inlet, which is mainly caused by the vortex formation and impact losses, respectively, as shown in Fig. 12a. After optimization, the energy dissipation is decreased obviously, and the position of the maximum energy dissipation is moved from the middle to the right side of branch D inlet, thereby reducing energy losses.

3.4 Flow Resistance

Tab. 5 lists the flow losses of the original and optimized cases. It can be clearly seen that after optimization, in addition to the branch C, the pressure drop of remaining four branch pipes is well balanced, so in actual operation, only the throttle valve on the branch C needs to be regulated. Moreover, the total pressure drop of branches A and E keeps unchanged, but that of branches B and D reduces greatly, and that of branch C decreases appreciably. For Case 1, the total pressure drop of branch B and D respectively reduces by about 15% and 42% compared to the original layout. For Case 2, the total pressure drop of branches B and C reduces by approximately 28% and 11%, respectively. For Case 3, the

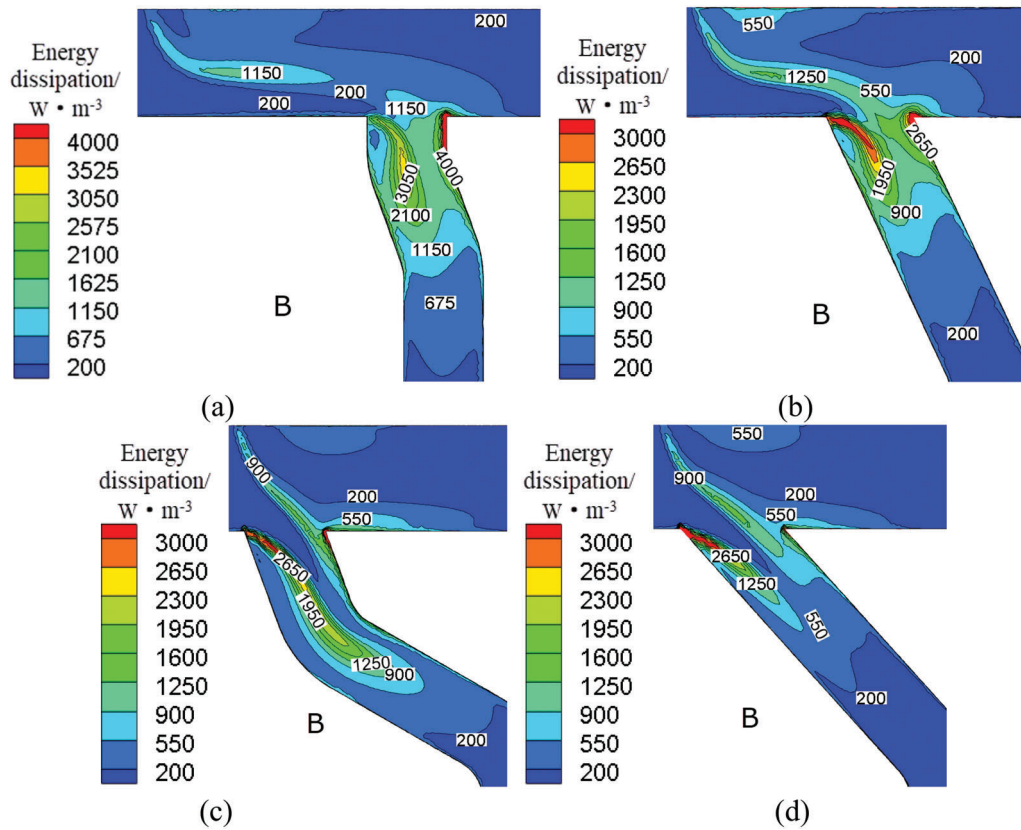


Figure 9: Energy dissipation distribution of Z-section at the inlet of branch B. (a) Original (b) Case 1 (c) Case 2 and (d) Case 3

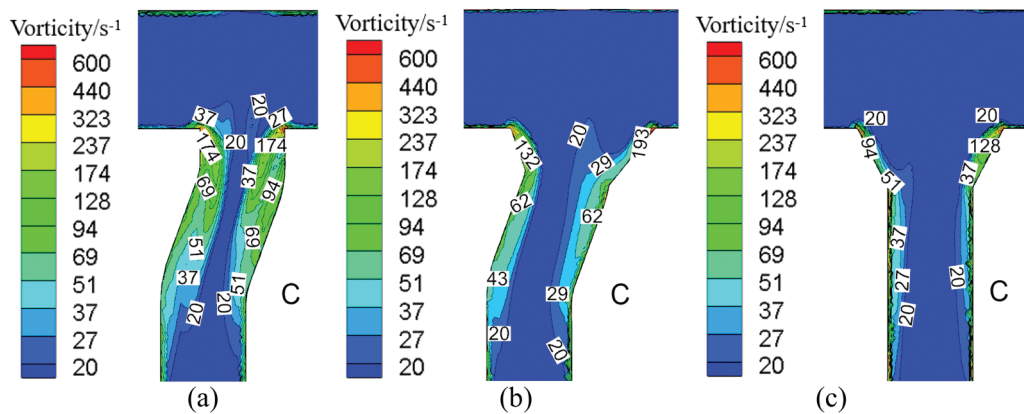


Figure 10: Vorticity distribution of Z-section at the inlet of branch C. (a) Original (b) Case 2 and (c) Case 3

total pressure drop of branches B and C reduces by approximately 48% and 14%, respectively. The above results indicate that the improvement of the flow patterns at the inlet of each branch and the reduction of vortex strength are the main reasons for the decrease in flow resistance. However, on the other hand, as the flow resistance of branch C is greatly affected by the upstream two tees, the reduction of flow resistance is very limited. It can be concluded here from the above analysis that Case 3 is a preferred selection for optimizing the hot primary-air pipe system in the practical utilization.

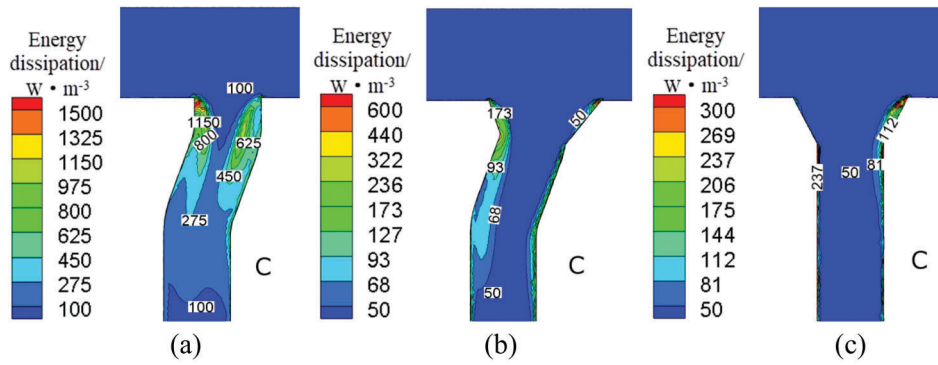


Figure 11: Energy dissipation distribution of Z-section at the inlet of branch C. (a) Original (b) Case 2 and (c) Case 3

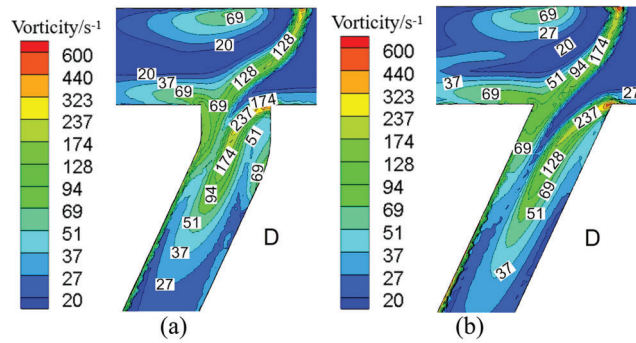


Figure 12: Vorticity distribution of Z-section at the inlet of branch D. (a) Original and (b) Case 1

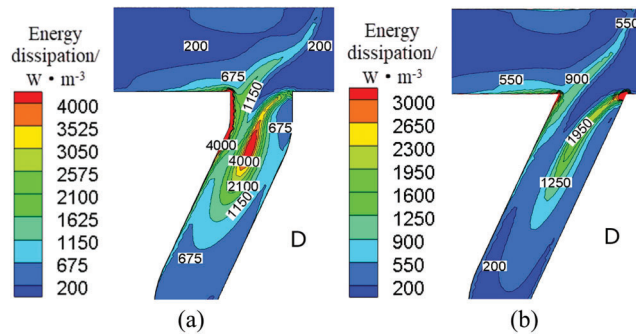


Figure 13: Energy dissipation distribution of Z-section at the inlet of branch D. (a) Original and (b) Case 1

Table 5: Total pressure drop of each branch

Type	Total pressure drop (Pa)				
	A	B	C	D	E
Original	295.5	560.4	504.9	574.8	287.9
Case 1	293.4	476.1	503.3	336.2	288.5
Case 2	295.8	405.5	447.6	334.1	287.6
Case 3	295.6	291.7	434.6	333.4	287.7

4 Conclusion

For the original layout of the hot primary-air pipe system, the total pressure is almost symmetrically distributed on the left and right sides of the header. A low-pressure recirculation zone is evolved on the downwind side of branches B and D, and the low-pressure circulation zone at branch D inlet is large, leading to the most significant flow losses, following by branches B and C with the large flow losses, and branches A and E with the small losses. For branch B pipe, the flow losses from the X-section to Y-section account for approximately 74% of the total losses of the pipe system.

After optimization, the flow losses of branch A and E are basically unchanged. The reduction of the flow losses of branch B in Cases 1 and 2 is low. However, for Case 3, the flow regime at the inlets of branches B, C, and D is improved greatly. The size and strength of vortex are significantly reduced, and compared with the original layout, the flow losses of branches B and D reduce by approximately 48% and 42%, respectively. As the flow losses of branch C are strongly affected by the upstream two tees, the flow losses only reduce by 14%. Case 3 is a preferred selection for optimizing the hot primary-air pipe system in the practical applications.

Funding Statement: The authors received no specific funding for this study.

Conflicts of Interest: The authors declare that they have no conflicts of interest to report regarding the present study.

References

1. Sambandam, M. T., Madloul, N. A., Saidur, R., Devaraj, D., Rajakarunakaran, S. (2017). Investigation of energy saving potentials in T-junction and elbow in compressed air systems. *Energy Efficiency*, 10(5), 1099–1113. DOI 10.1007/s12053-016-9493-0.
2. Li, A., Chen, X., Chen, L. (2014). Numerical investigations on effects of seven drag reduction components in elbow and T-junction close-coupled pipes. *Building Services Engineering Research and Technology*, 36(3), 295–310. DOI 10.1177/0143624414541453.
3. Duan, J. H., Fang, L., Gao, S., Zhang, Z. S., Wang, W. (2019). Numerical simulation and structural optimization of multi-compartment fluidized bed reactor for biomass fast pyrolysis. *Chemical Engineering and Processing—Process Intensification*, 140, 114–126. DOI 10.1016/j.cep.2019.05.004.
4. Zhang, W. Q., Li, A. G., Gao, R., Li, C. (2018). Effects of geometric structures on flow uniformity and pressure drop in dividing manifold systems with parallel pipe arrays. *International Journal of Heat and Mass Transfer*, 127, 870–881. DOI 10.1016/j.ijheatmasstransfer.2018.07.111.
5. Kou, J. L., Chen, Y. Y., Zhou, X. Y., Lu, H. J., Wu, F. M. et al. (2014). Optimal structure of tree-like branching networks for fluid flow. *Physica A: Statistical Mechanics and Its Applications*, 393, 527–534. DOI 10.1016/j.physa.2013.08.029.
6. Zhou, J., Sun, Z. N., Ding, M., Bian, H. Z., Zhang, N. et al. (2017). CFD simulation for flow distribution in manifolds of central-type compact parallel flow heat exchangers. *Applied Thermal Engineering*, 126, 670–677. DOI 10.1016/j.applthermaleng.2017.07.194.

7. Jiang, Y. G., Xu, Y. X., Qin, J., Zhang, S. L., Chetehouna, K. et al. (2018). The flow rate distribution of hydrocarbon fuel in parallel channels with different cross section shapes. *Applied Thermal Engineering*, 137, 173–183. DOI 10.1016/j.applthermaleng.2018.03.033.
8. Li, S., Liu, X. F., Wang, J. X., Zheng, Y. L., Deng, S. M. (2019). Experimental reduced-scale study on the resistance characteristics of the ventilation system of a utility tunnel under different pipeline layouts. *Tunnelling and Underground Space Technology*, 90, 131–143. DOI 10.1016/j.tust.2019.04.021.
9. Zhang, W. Q., Li, A. G. (2018). Resistance reduction via guide vane in dividing manifold systems with parallel pipe arrays (DMS-PPA) based on analysis of energy dissipation. *Building and Environment*, 139, 189–198. DOI 10.1016/j.buildenv.2018.04.010.
10. Costa, N. P., Maia, R., Proença, M. F., Pinho, F. T. (2006). Edge effects on the flow characteristics in a 90deg Tee junction. *Journal of Fluids Engineering*, 128(6), 1204–1217. DOI 10.1115/1.2354524.
11. Beneš, L., Louda, P., Kozel, K., Keslerová, R., Štigler, J. (2013). Numerical simulations of flow through channels with T-junction. *Applied Mathematics and Computation*, 219(13), 7225–7235. DOI 10.1016/j.amc.2011.04.074.
12. Li, A. G., Chen, X., Chen, L., Gao, R. (2013). Study on local drag reduction effects of wedge-shaped components in elbow and T-junction close-coupled pipes. *Building Simulation*, 7(2), 175–184. DOI 10.1007/s12273-013-0113-z.
13. Gao, R., Wen, S. H., Li, A. G., Zhang, H. C., Du, W. Y. et al. (2019). A novel low-resistance damper for use within a ventilation and air conditioning system based on the control of energy dissipation. *Building and Environment*, 157, 205–214. DOI 10.1016/j.buildenv.2019.04.041.
14. Ye, X. M., Li, P. M., Li, C. X., Ding, X. L. (2015). Numerical investigation of blade tip grooving effect on performance and dynamics of an axial flow fan. *Energy*, 82, 556–569. DOI 10.1016/j.energy.2015.01.065.
15. Ye, X. M., Zhang, J. K., Li, C. X. (2017). Effect of blade tip pattern on performance of a twin-stage variable-pitch axial fan. *Energy*, 126, 535–563. DOI 10.1016/j.energy.2017.03.057.
16. Hao, C. Z., Song, X. M., Jia, Z. N. (2019). Influence of the hole chamfer on the characteristics of a multi-hole orifice flowmeter. *Fluid Dynamics & Materials Processing*, 15(4), 391–401. DOI 10.32604/fdmp.2019.07771.
17. Cheng, X. R., Chen, H. X., Wang, X. Q. (2019). Analysis of the impact of the space guide vane wrap angle on the performance of a submersible well pump. *Fluid Dynamics & Materials Processing*, 15(3), 271–284. DOI 10.32604/fdmp.2019.07250.
18. Bentarzi, F., Mataoui, A. (2018). Turbulent flow produced by twin slot jets impinging a wall. *Fluid Dynamics & Materials Processing*, 14(2), 107–120.
19. Rahmeyer, W. J., Dent, P. (2003). Pressure loss data for PVC pipe tees. *ASHRAE Transactions*, 109(2), 252–271.
20. Gao, R., Liu, K. K., Li, A. G., Fang, Z. Y., Yang, Z. G. et al. (2018). Study of the shape optimization of a tee guide vane in a ventilation and air-conditioning duct. *Building and Environment*, 132, 345–356. DOI 10.1016/j.buildenv.2018.02.006.